



High temperature polybenzimidazole membrane electrode assemblies using pyridine-polybenzimidazole as catalyst layer binder

Po-Hao Su ^a, Joy Cheng ^a, Jia-Fen Li ^a, Yi-Hsiang Liao ^a, T. Leon Yu ^{a,b,*}

^a Department of Chemical Engineering & Materials Science, Yuan Ze University, Chung-Li, Taoyuan 32003, Taiwan

^b Fuel Cell Center, Yuan Ze University, Chung-Li, Taoyuan 32003, Taiwan



HIGHLIGHTS

- Higher pyridine content catalyst binder enhances catalyst layer H₃PO₄ loading.
- Higher pyridine content catalyst binder enhances fuel cell performance.
- Higher pyridine content catalyst binder enhances H₃PO₄ binding sites.

ARTICLE INFO

Article history:

Received 20 September 2013

Received in revised form

7 February 2014

Accepted 27 February 2014

Available online 18 March 2014

Keywords:

Poly(benzimidazole)

Pyridine-polybenzimidazole

Catalyst layer

Proton exchange membrane fuel cell

ABSTRACT

We synthesize four pyridine-polybenzimidazoles (PyPBIs) and one polybenzimidazole (PBI) from a tetraamin monomer (i.e., 3,3'-diamino benzidine (DABZ)) and two dicarboxylic acid monomers (i.e., isophthalic acid (IPA) and 2,6-pyridinedicarboxylic acid (PyA)) with PyA/IPA molar ratios of 6/4 (i.e., PyPBI-64), 5/5 (i.e., PyPBI-55), 4/6 (i.e., PyPBI-46), 3/7 (i.e., PyPBI-37), and 0/1 (i.e., PBI-11). The PyPBIs and PBI with molecular weight of $\sim 1.0\text{--}1.3 \times 10^{-4}$ g mol⁻¹ are used as Pt–C (Pt on carbon support) binders for fabricating gas diffusion electrodes (GDEs) and are doped with H₃PO₄ to prepare membrane electrode assemblies (MEAs). We demonstrate that both the H₃PO₄ loading of the GDE and the fuel cell performance of the MEA at 160 °C with unhumidified H₂/O₂ fuel increase with the increase of PyA monomer content of the PyPBI (or PBI) binder in the GDEs according to the sequence of PBI-11 < PyPBI-37 < PyPBI-46 < PyPBI-55 < PyPBI-64. The higher PyA content PyPBI provides more binding sites for H₃PO₄ in GDE and enhances fuel cell performance.

© 2014 Elsevier B.V. All rights reserved.

1. Introduction

The proton exchange membrane fuel cell (PEMFC) is considered as one of the most promising next generation clean energy technologies, because of its high efficiency and non-polluting nature. In the past two decades, researchers [1–5] have made efforts to develop hydrocarbon membranes for PEMFCs working at high temperatures. Compared to Nafion-based low temperature PEMFCs, the high temperature PEMFCs (HT-PEMFCs, 120 °C < Temp < 200 °C) have the following advantages: higher rapid electrode kinetics, greater tolerance to the CO impurities in the hydrogen fuel stream, and easy water–thermal management [6,7]. One of the most promising proton exchange membranes

(PEMs) suitable for HT-PEMFCs is the polybenzimidazole doped phosphoric acid (PBI/H₃PO₄) membrane [1,2], in which H₃PO₄ acts as proton-conducting carrier, and no water is needed for proton-conduction in the membranes. The PBI/H₃PO₄ membrane has shown to possess high proton conductivity at 120–200 °C with low humidity, good mechanical strength, excellent chemical and thermal stability, and is employed with greater success than other PEMs in HT-PEMFCs [8,9].

The combination of an effective contact at the three-phase boundary, that is, high Pt catalyst utilization, good proton conduction, and facile H₂ and O₂ (or air) transport to the Pt active sites in the catalyst layer (CL), is necessary for a high-performance membrane electrode assembly (MEA) [10,11]. The MEA of a PBI/H₃PO₄ based HT-PEMFC consists of a PBI/H₃PO₄ PEM, anode and cathode CLs, and gas diffusion layers (GDLs). The three major components of a CL are: Pt–C (Pt on a carbon support), H₃PO₄, and PBI, in which H₃PO₄ acts as a proton conductor, PBI serves as a binder of Pt–C and also as an ionomer for fixing H₃PO₄ in the CL to avoid leakage of H₃PO₄ from the CL to the GDL. The concentrations of the H₃PO₄ and PBI ionomer

* Corresponding author. Department of Chemical Engineering & Materials Science, Yuan Ze University, Chung-Li, Taoyuan 32003, Taiwan. Tel.: +886 3 4638800x2553; fax: +886 3 4559373.

E-mail address: cetyl@saturn.yzu.edu.tw (T.L. Yu).

in the CLs as well as the microstructure morphology of the Pt–C, PBI, and H₃PO₄ components play important roles in determining the properties and performance of CLs [12–21].

In an HT-PEMFC, a high concentration of H₃PO₄ is necessary to achieve sufficient proton conductivity within the PEM and the CLs. Thus a good ionomer catalyst binder for retaining H₃PO₄ in CL is an important issue for a high performance HT-PEMFC. In this study, instead of using PBI binder, we used pyridine-polybenzimidazole (PyPBI) as a Pt–C catalyst binder for fabricating gas diffusion electrodes (GDEs) of PBI/H₃PO₄-based MEAs. Four PyPBIs synthesized from a tetramin monomer (i.e., 3,3'4,4'-diamino biphenyl (DABZ)) and two dicarboxylic acid monomers (i.e., 2,6-pyridinedicarboxylic acid (PyA) and isophthalic acid (IPA)) with initial [PyA]/[IPA] fed molar ratios of 6/4–3/7, and one PBI synthesized from DABZ and IPA (see the chemical reaction scheme in Fig. 1). We demonstrated that the PyA pyridine group in the PyPBI binder enhances the binding of H₃PO₄ molecules in CLs and raises the fuel cell performance.

Comparing with the Nafion-based GDEs, in which water and Nafion ionomer are proton conductors, the kinetics for O₂ reduction on Pt–C within the pure H₃PO₄ is slow because of the strong adsorption effect of H₃PO₄ and H₂PO₄[−] on the Pt active sites and the low solubility and diffusivity of the O₂ in pure H₃PO₄ [22]. Li et al. reported that a combination of H₃PO₄ with PBI can increase the O₂ solubility and suppress adsorption of H₃PO₄ and H₂PO₄[−] on the Pt-active sites, thus enhancing the Pt catalytic activity of O₂ reduction [23]. In the present study, we fabricated GDEs using low molecular weight (MW, M_w = 1.0–1.3 × 10⁴ g mol^{−1}) PyPBI and PBI binders mixed with Pt–C, LiCl, and N,N'-dimethyl acetamide (DMAc) solvent catalyst ink solutions. The low MW PyPBI (or PBI) binders and LiCl reduce inter-polymer hydrogen bonding of PyPBI (or PBI) and help dispersion of PyPBI (or PBI) in the catalyst ink solutions [24] and in CLs. As a result, there is an increase in the PyPBI (or PBI) binding sites for H₃PO₄ molecules in the CLs and Pt catalytic activity is enhanced [25]. In all the MEAs, the [Pt–C]/[PyPBI (or PBI)] weight ratio in a CL was fixed at 19/1, which was similar in value to the [Pt–C]/[PBI] weight ratio of 20/1 suggested in the literature [14,26]. In this study, we used a high MW PBI (M_w = 1.74 × 10⁵ g mol^{−1}) cross-linked with epoxy resin to prepare membranes. These cross-linked PBI membranes were doped with H₃PO₄ and were used as PEMs for fabricating MEAs [27].

2. Experimental

2.1. PBI synthesis

PBI was synthesized from DABZ (Aldrich Chem. Co.) and IPA (Aldrich Chem. Co.) using polyphosphoric acid (PPA, Aldrich

Table 1
Monomer fed quantities for PyPBIs and PBI syntheses.

Sample designation	DABZ mole (g)	PyA mole (g)	IPA mole (g)	Initial fed C:N:H ^a	Polymer ^b C:N:H ^b
PyPBI-64	1.0 (214)	0.6 (100)	0.4 (66)	1.00:0.283:0.09	1.00:0.278:0.09
PyPBI-55	1.0 (214)	0.5 (84)	0.5 (83)	1.00:0.277:0.09	1.00:0.268:0.09
PyPBI-46	1.0 (214)	0.4 (67)	0.6 (100)	1.00:0.270:0.09	1.00:0.256:0.09
PyPBI-37	1.0 (214)	0.3 (50)	0.7 (116)	1.00:0.265:0.09	1.00:0.247:0.09
PBI	1.0 (214)	0.0	1.0 (166)	1.00:0.246:0.09	1.00:0.229:0.09

^a Elemental analyses data of synthesized polymers.

^b C:N:H in atomic ratio.

Chem. Co.) as a solvent. The detailed polymerization procedures were similar to those reported in the literature [27,28]. 4200 g PPA was mixed with DABZ and melted at 200 °C under a N₂ atmosphere for more than 3 h to obtain a homogeneous mixture. Subsequently, IPA was mixed into the solution to initiate polymerization. The quantities of the monomers fed into the reaction flask for PBI synthesis are listed in Table 1. The PBI was polymerized under a N₂ atmosphere at 210 °C for 48 h. After terminating the polymerization, the product mixture was poured into distilled water to precipitate the PBI product. The precipitated PBI was milled into a powder and then mixed with a 1 N NaOH aqueous solution under stirring for 2 h. During stirring, the NaOH aqueous solution was exchanged every 30 min to remove residual PPA. The PBI was subsequently rinsed with deionized water several times to remove residual NaOH and then dried under vacuum at 120 °C for 4 h.

2.2. Fractionation of the as-synthesized PBI to obtain a low MW and a high MW PBIs

The as-synthesized PBI, obtained in Section 2.1, was fractionated by solvent extraction using an N-methylformamide (NMF; a poor solvent of PBI) and N-methyl pyrrolidinone (NMP; a good solvent of PBI) mixture to obtain a low MW PBI. A 16 g mass of the as-synthesized PBI was added to a solvent mixture comprising 35 g of NMF (Aldrich Chemical Co.) and 15 g of NMP (Aldrich Chemical Co.) and stirred at 30 °C for 3 h. The resulting solution was then filtered to obtain filtrate and residual solid. The solvent of the filtrate was evaporated at 150 °C under vacuum for 2 h to obtain the solid PBI-11, which had a weight average MW of M_w = 1.1 × 10⁴ g mol^{−1} determined as described in Section 2.5. The residual solid was designated as PBI-174, which had a M_w = 1.74 × 10⁵ g mol^{−1}. The MWs of PBI-11 and PBI-174 were determined using a GPC as described in Section 2.5.

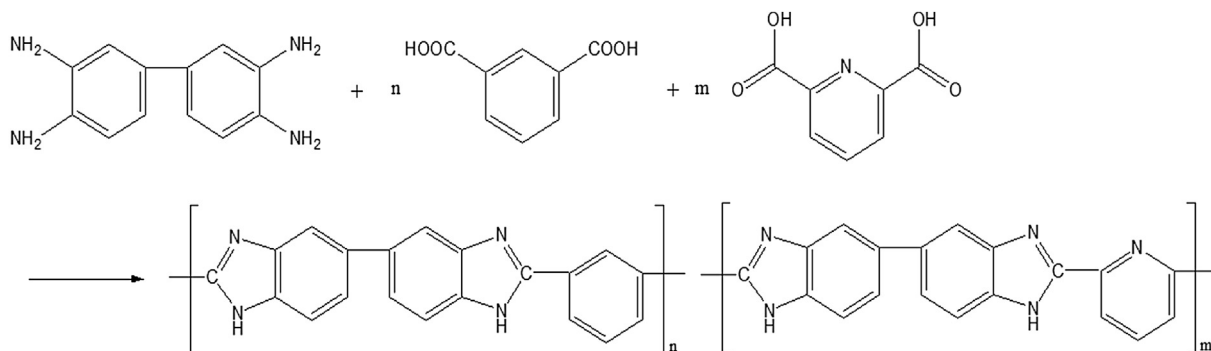


Fig. 1. Reaction scheme of PyPBI from a tetramin monomer, i.e., 3,3'-4,4'-tetraminbiphenyl (DABZ), and two dicarboxylic acid monomers, i.e., isophthalic acid (IPA) and 2,6-pyridinedicarboxylic acid (PyDA).

2.3. Syntheses of four PyPBIs

PyPBIs were synthesized from DABZ monomer and two dicarboxylic acid monomers, that is, IPA and PyA, with [PyA]/[IPA] molar ratios of 3/7, 4/6, 5/5, and 6/4 and the [DABZ]/[PyA + IPA] molar ratio of 1/1. The quantities of the monomers fed into the reaction flask for PyPBI syntheses are also listed in Table 1. The reaction scheme is shown in Fig. 1. The DABZ monomer was mixed with 4200 g PPA solvent at 200 °C under N₂ gas for 3 h. IPA was then fed into the flask and the temperature was maintained at 210 °C for 4 h. Subsequently, PyA was fed into the flask and further reaction proceeded for 6 h. The total reaction time at 210 °C was 10 h, which was shorter than that of PBI synthesis, which was 48 h. The shorter polymerization time led the as-synthesized PyPBIs to have MWs ($M_w = \sim 1.0\text{--}1.3 \times 10^4 \text{ g mol}^{-1}$, determined as described in Section 2.5) smaller than the as-synthesized PBI ($M_w = \sim 17.4 \times 10^4 \text{ g mol}^{-1}$, determined as described in Section 2.5). The hot reaction product was poured into a beaker containing a large quantity of distilled water. The precipitate was rinsed with distilled water and then mixed with NaOH aqueous solution to dissolve out the phosphoric acid and obtain the PyPBI product. The procedure was similar to the PBI synthesis described in Section 2.1.

2.4. Elemental analyses of PyPBIs and PBI-11

The C, N, and H elemental analyses of four PyPBIs and PBI-11 were carried out using an Elemental Analyzer (Vario EL/micro cube, Elementar Co., Germany). Table 1 summarizes the atomic ratios of the four PyPBIs and PBI-11 obtained by C:N:H elemental analyses and the initially fed monomer C:N:H atomic ratios for PyPBIs and PBI syntheses. The elemental analyses results indicated that the element compositions of the final synthesized polymers were similar to the initial monomer reactants fed for polymerization, and the N atom content increased according to the sequence of PBI < PyPBI-37 < PyPBI-46 < PyPBI-55 < PyPBI-64.

2.5. MW distribution determinations of PyPBIs and PBIs

The MW distributions of PBI-174, PBI-11, obtained in Section 2.2, and four PyPBIs, obtained in Section 2.3, were determined at 40 °C using a gel permeation chromatography (GPC, Jasco PU-2080 plus) with refractive index (RI) detector (Jasco RI-2031 plus). DMAc was used as the mobile phase and the concentration of each PyPBI and PBI elution solution was $\sim 1.0 \text{ mg mL}^{-1}$. To prevent PBI (or PyPBI) aggregation, $\sim 1.0 \text{ mg mL}^{-1}$ of LiCl was mixed into the PBI/DMAc and PyPBI/DMAc elution solutions. The solution flow rate was 0.8 mL min^{-1} . Narrow MW distribution polystyrene standards ($M_w/M_n \leq 1.1$, Aldrich) were used for the GPC MW calibration.

2.6. FTIR characterization of PyPBIs and PBI

Infrared (IR) spectra of PBI-11 and four PyPBIs were obtained using a Perkin–Elmer 1725X Fourier transform infrared spectroscopy (FTIR). Each solid PBI and PyPBI powder was mixed and milled with KBr to make IR sample.

2.7. Gas diffusion electrode (GDE) preparations

The four PyPBIs (i.e., PyPBI-64, PyPBI-55, PyPBI-46, and PyPBI-37) and PBI-11 were used to prepare catalyst ink solutions and to fabricate GDEs. All these PyPBIs and the PBI-11 had MWs of $\sim 1.0\text{--}1.3 \times 10^4 \text{ g mol}^{-1}$ (see Table 2). The fabrication materials comprised Pt–C (Pt content 40 wt%, Johnson Matthey Co.) catalyst, a carbon paper GDL (35 BC, SGL Co.), PBI (or PyPBI) binder, and DMAc solvent. Each catalyst ink solution was composed of [Pt–C]/[PBI] (or

Table 2

GPC molecular weights of PBIs and Py-PBIs (estimated using polystyrene standard calibrations).

Sample	$M_w (\text{g mol}^{-1})$	M_w/M_n
PyPBI-64	1.27×10^4	1.29
PyPBI-55	1.30×10^4	1.12
PyPBI-46	1.18×10^4	1.13
PyPBI-37	1.09×10^4	1.04
PBI-11	1.10×10^4	1.13
PBI-174	17.4×10^4	2.14

PyPBI)]/[LiCl]/[DMAc] at a weight ratio of 9.5/0.5/0.5/190. LiCl was mixed into each catalyst ink solution to enhance PBI (or PyPBI) dispersion in the DMAc solvent [24]. Each catalyst ink solution underwent ultrasonic treatment for 5 h. The solution was then coated on a GDL using an ultrasonic spray system (Sono Tek Co., NY). Finally, the solvent in the coated CL was evaporated at 80 °C for 1 h and then at 150 °C under vacuum for 1 h. The GDL coated with a CL was then immersed in distilled water for 20 min. The procedure was repeated several times by exchanging fresh distilled water to remove the LiCl. Subsequently, the GDE was dried under vacuum at 60 °C for 1 h to remove residual water.

2.8. Pt-electrochemical active surface area (Pt-ECSA) measurements of GDEs

The GDEs prepared according to the procedures described in Section 2.7 were used for Pt-ECSA measurements. Each GDE sample comprised a Pt loading of 0.1 mg cm^{-2} with an active area of $1 \times 2 \text{ cm}^2$. ECSA measurements were performed using a three-electrode system in a container filled with a 0.5 M H₂SO₄ aqueous solution. A saturated calomel electrode (SCE) connected with a salt bridge was used as a reference electrode, a platinum wire was used as a counter electrode, and the GDE was used as a working electrode. The measurements were conducted using cyclic voltammetry (CV; CHI611C Electrochemical Analyzer, CH Instruments) with a scan rate of 50 mV s^{-1} versus a normal hydrogen electrode (NHE) at 25 °C. During testing, the H₂SO₄ solution was fed with humidified N₂ at a pressure of 40 psi. The Pt specific ECSA was calculated using the equation: $\text{ECSA} = Q_H/(m \times q_H)$, where Q_H is the charge exchanged during the electro-adsorption of H₂ on Pt, m is the Pt loading quantity, and q_H ($210 \mu\text{C cm}^{-2}$) is the charge required for the monolayer adsorption of H₂ on Pt surfaces [29,30].

2.9. PBI MEA preparations

2.9.1. Membrane preparation and characterizations

The high MW PBI-174, was blended with an epoxy resin (i.e., Epon-828, diglycidyl ether bisphenol-A) to create a cross-linked membrane [27]. The PBI-174/epoxy blend solution with an imidazole-NH/epoxide equivalent (Eqv.) number ratio of 10/1 (where the imidazole-NH Eqv. wt. of PBI and the epoxide Eqv. wt. of Epon 828 were 154 g/NH Eqv. and 193 g/epoxide Eqv., respectively) was prepared using DMAc solvent. The polymer concentration of each solution was approximately 5.0 wt%. The membrane was prepared by casting the solution onto a glass plate using a blade coater. The cast solution film was then dried under vacuum at 80 °C for 24 h followed by heating at 135 °C for 1 h to remove the solvent and to proceed with epoxide-PBI cross-linking reaction. The thickness (L) of the membrane was $\sim 50 \mu\text{m}$. The membrane was doped with H₃PO₄ by immersion in an 85 wt% phosphoric acid aqueous solution at 70 °C for 48 h. The H₃PO₄ doping level (PA_{dop}) of the membrane was $\text{PA}_{\text{dop}} = 5.9 \pm 0.3 \text{ mol H}_3\text{PO}_4 \text{ per PBI repeat unit}$; this value was defined as the number of moles of H₃PO₄ doped

into 1 mol of PBI repeat unit and was calculated from the equation $PA_{dop} = [(W_1 - W_0)/98]/[xW_0/308]$, where W_0 is the weight of the dry membrane, x is the weight fraction of PBI in the cross-linked membrane, W_1 is the weight of a membrane containing doped phosphoric acid, and the values 98 and 308 are the MWs of H_3PO_4 and the PBI repeat unit, respectively. To avoid measurement error because of moisture content, the membranes were dried by heating at 110 °C under vacuum for more than 10 h prior to weighing until a constant weight was obtained. The PA_{dop} datum was the average of three measurements.

The ionic conductivity (σ) of the membrane was $\sigma = (1.35 \pm 0.04) \times 10^{-2} \text{ S cm}^{-1}$ and was calculated from the equation: $\sigma = L/(A \times R)$, where $A = 3.14 \text{ cm}^2$ is the cross sectional area of the membrane for a resistance R measurement. Through-plane R values were measured by alternating current (AC) impedance spectroscopy using a Solartron 1260 gain phase analyzer interfaced to a Solartron 1480 multimeter. The membrane was secured in a holder located between two probes for the R measurement. The entire testing setup was kept in a thermostat at 160 °C with 0.0 %RH (relative humidity). The datum was the average of three measurements.

2.9.2. MEA preparation

The PBI/epoxy cross-linked membrane prepared in Section 2.9.1 and the GDEs prepared according to the procedures described in Section 2.7 were used for the MEA preparation. The Pt loading of the GDEs at both the anode and cathode was 0.5 mg cm^{-2} , and the GDE active area was $3.5 \times 3.5 \text{ cm}^2$. The GDEs were doped with H_3PO_4 by immersion in 10 wt% H_3PO_4 aqueous solution at room temperature for 12 h and subsequently dried in an oven at 110 °C for 2 h. Two GDEs prepared using the same catalyst ink solution were placed on either side of a PBI/epoxy cross-linked PEM and pressed at 130 °C with a pressure of 50 N cm^{-2} for 1 min to obtain an MEA. The H_3PO_4 loading of each GDE was estimated from the weight difference of the GDE before and after doping with H_3PO_4 . The GDE before and after doping with H_3PO_4 was dried under vacuum at 120 °C for 2 h to evaporate moisture prior to estimating the H_3PO_4 loading of a GDE.

2.10. Unit fuel cell tests and impedance measurements

The performance of the unit cells was tested at 160 °C and ambient pressure using an FC5100 fuel cell testing system (CHINO Inc., Japan). The flow rates of non-humidified H_2 , O_2 , and air were set to 200, 200, and 1000 mL min^{-1} , respectively. The i - V (current density vs. cell voltage) curves were obtained after the fuel cell was operated for 8 h by measuring the current density as a function of cell voltage at decrementing intervals of 0.05 V. The duration of each i - V measurement was 30 s. The impedances of the MEAs were measured at $i = 200 \text{ mA cm}^{-2}$ and 1000 mA cm^{-2} using the same fuel cell test system with unhumidified H_2 and O_2 gases which were both operated at a flow rate of 200 mL min^{-1} . The frequency response analyzer was a Model 850e Fuel Cell Test System (Scribner Associates, Inc.) and the scanning frequency ranged from 10^4 Hz to 0.1 Hz. Cell internal resistances of the MEAs were also determined using current interrupt method [31].

3. Results and discussion

3.1. MW distributions of PBIs and PyPBIs

The MW distributions of the as-synthesized PyPBIs, that is, PyPBI-64, PyPBI-55, PyPBI-46, and PyPBI-37, and the PBI-174 and PBI-11, which were fractionated from the as-synthesized PBI using a NMF/NMP solvent mixture, were determined using GPC analyses.

Fig. 2 illustrates the polystyrene standard-calibrated GPC MW distributions of the four PyPBIs and two PBIs. The M_w and M_w/M_n values of these six polymers were estimated from the GPC data (Fig. 2) and are summarized in Table 2. In this study, the PBI-11 and four PyPBIs, which had M_w s of $\sim 1.0\text{--}1.3 \times 10^4 \text{ g mol}^{-1}$, were used as Pt-C catalyst binder and MEA CL fabrications. The PBI-174, which had a $M_w = 1.74 \times 10^5 \text{ g mol}^{-1}$, was used for preparing PEMs.

3.2. Infrared spectra of PBI and four PyPBIs

Fig. 3 illustrates the IR spectra of IPA monomer, PyA monomer, PyPBI-64, PyPBI-55, PyPBI-46, PyPBI-37, and PBI-11. The peak around 1690–1700 cm^{-1} of PyDA (spectrum-a) and IPA (spectrum-g) is because of the absorption of $-\text{C=O}$ stretch of the carboxylic acid functional group. The spectra -g and -a also show that the C=O stretch ($\sim 1690 \text{ cm}^{-1}$) absorption overlaps with the benzene ring C=C stretch absorption at $\sim 1610 \text{ cm}^{-1}$. The 1690–1700 cm^{-1} C=O stretch absorption peak is not visible in the IR spectra of PyPBIs (spectra b-e) and PBI (spectrum-f) because of the conversion of C=O group to imidazole C=N group after polymerization. The absorption peak at $\sim 1574 \text{ cm}^{-1}$ of PyA (spectrum-a) can be attributed to the absorption of pyridine C=N stretch. The C=N stretch absorption $\sim 1560\text{--}1600 \text{ cm}^{-1}$ is also observed overlapping with the C=C stretch absorption at $\sim 1610 \text{ cm}^{-1}$ in the spectra of PyA (spectrum a), PyPBIs (spectra b-e), and PBI-11 (spectrum f). The absorption at $\sim 1420 \text{ cm}^{-1}$ in the spectrum of IPA (spectrum-g) and $\sim 1412 \text{ cm}^{-1}$ in the spectrum of PyA (spectrum-a) is the in plane C=C deformation absorption of benzene ring, and the absorption at $\sim 1456 \text{ cm}^{-1}$ in the spectra of PyA (spectrum-a) is the C=N in plane deformation absorption of pyridine [32,33]. In Fig. 3, we used blue dashed lines to indicate the PyA C=N stretch ($\sim 1574 \text{ cm}^{-1}$) and C=N in plane deformation ($\sim 1456 \text{ cm}^{-1}$) absorptions of spectrum-a, for easy viewing of the shifting of PyPBI-64 (spectrum-b) to PBI-11 (spectrum-f) of the C=N stretch ($\sim 1574 \text{ cm}^{-1}$) and C=N ($\sim 1456 \text{ cm}^{-1}$) in plane deformation absorptions with the decreasing of PyA monomer content in PyPBIs. In the spectrum of PyPBI-64 (spectrum-b), we can observe that the 1566 cm^{-1} C=N stretch and 1453 cm^{-1} C=N in plane deformation absorptions of

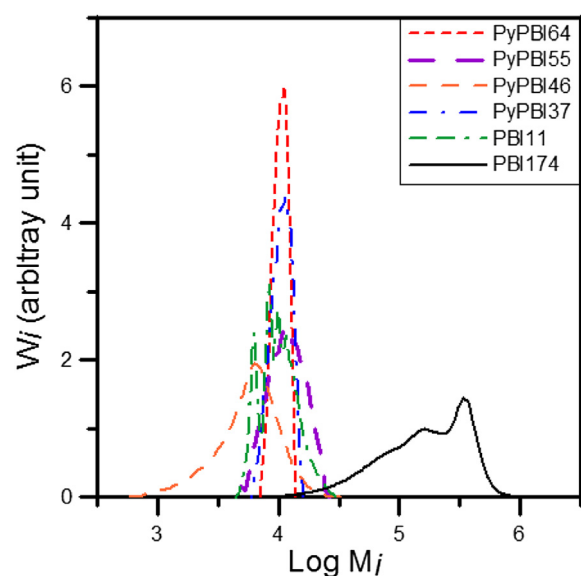


Fig. 2. GPC molecular weight distribution curves of PBIs and PyPBIs. Narrow molecular weight distribution polystyrene standards were used in the molecular weight calibration. (—) PyPBI-64; (—) PyPBI-55; (—) PyPBI-46; (—·—) PyPBI-37; (—·—) PBI-11; (—) PBI-174.

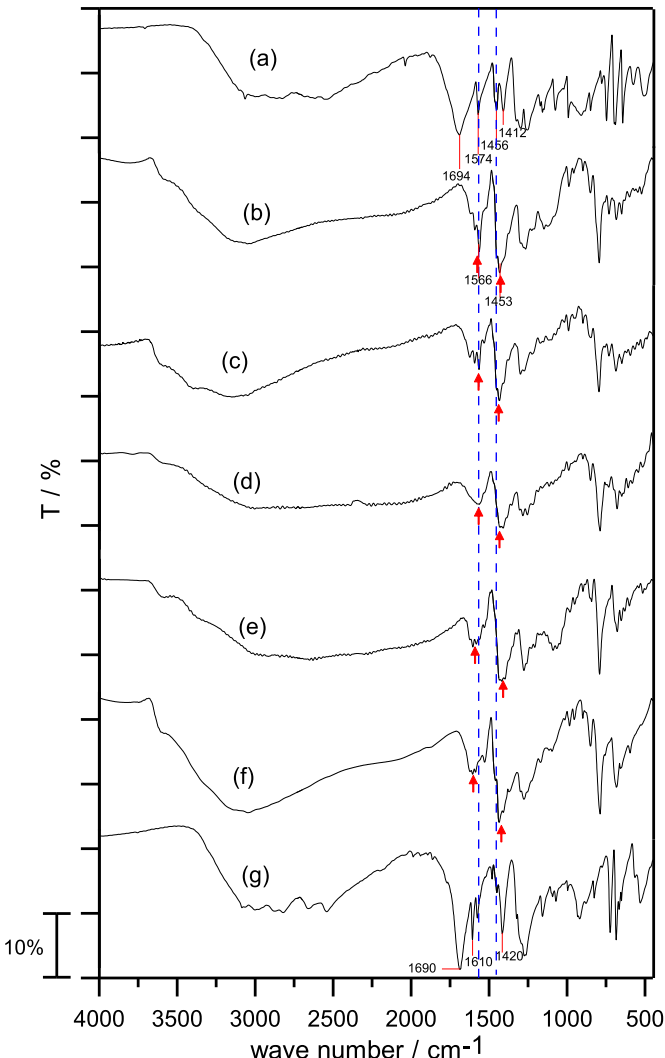


Fig. 3. IR spectra. (a) 2,6-pyridinedicarboxylic acid (PyA) monomer; (b) PyPBI-64; (c) PyPBI-55; (d) PyPBI-46; (e) PyPBI-37; (f) PBI-11; (g) isophthalic acid (IPA) monomer. The blue dashed lines indicate the PyA (spectrum-a) C=N stretch (1574 cm^{-1}) and C=N in plane deformation (1456 cm^{-1}). (For interpretation of the references to colour in this figure legend, the reader is referred to the web version of this article.)

imidazole group overlap with the imidazole/or benzene ring C=C stretch and C=C in plane deformation absorptions, respectively. Carefully inspecting the IR spectra from spectrum-b (PyPBI-64) to spectrum-f (PBI-11), we found that the C=N stretch peak shifted from 1566 cm^{-1} to higher wave number closing to the C=C stretch absorption (1610 cm^{-1}) and the C=N in plane deformation peak shifted from 1453 cm^{-1} to lower wave number closing to the C=C in plane deformation (1420 cm^{-1}). This indicated that the C=N group content (i.e., PyA monomer content) of the polymers decreased from PyPBI-64 to PyPBI-37, and to PBI-11. These results were consistent with the initially fed PyA and IPA monomer ratios of the PyPBIs and PBI syntheses as shown in Table 1.

3.3. Pt-ECSA studies of GDEs without H_3PO_4 doping

Four PyPBIs (i.e., PyPBI-64, PyPBI-55, PyPBI-46, and PyPBI-37) and PBI-11 electrolyte binder were mixed with Pt-C and DMAc solvent to prepare Pt-C/PyPBI (or PBI) catalyst ink solutions and fabricated GDEs for Pt-ECSA studies. The Pt loading of each GDE was 0.1 mg cm^{-2} , and the wt. ratio of [PyPBI]/[Pt-C + PyPBI] (or [PBI]/

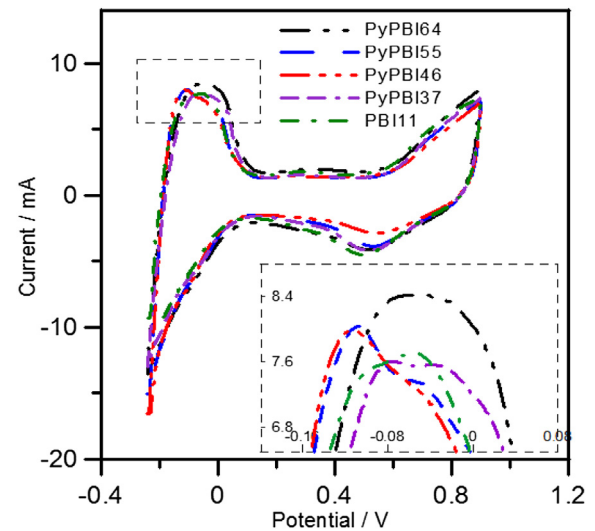


Fig. 4. Cyclic voltammetry (CV) curves of four Pt-C/PBI GDEs prepared from catalyst ink solutions containing PBI-11 and PyPBIs. The composition of each catalyst ink solution was Pt-C/PBI (or PyPBI)/LiCl/DMAc = 9.5/0.5/0.5/190 by wt. Polymer binders: (—) PyPBI-64; (—) PyPBI-55; (—) PyPBI-46; (—) PyPBI-37; (—) PBI-11.

[Pt-C + PBI]) of each GDE was 5 wt.%. Fig. 4 presents the CV curves of the five GDEs. Table 3 summarizes the Pt-ECSA estimates calculated from the CV data shown in Fig. 4. These data demonstrate that the Pt-ECSA of the GDE increases with increasing the PyA monomer content of the PyPBI (or PBI) binder in the catalyst inks according to the sequence of PBI-11 < PyPBI-37 < PyPBI-46 < PyPBI-50 < PyPBI-64. The reason for the increasing Pt-ECSA of GDE with increasing PyA monomer content of the PyPBI ionomer binder is not clear to us. The Pt-ECSA measurements were carried out in a $0.5\text{ M H}_2\text{SO}_4$ solution using CV, and the Pt-ECSA was estimated from the charge exchange of the electro-adsorption of H_2 on Pt. Fig. 5a (top reaction scheme) shows the interaction of an H^+ ion with the Pt particles on the surface of a carbon powder. A negatively charged electron on the carbon powder causes the attraction of an H^+ ion on to the surface of a Pt particle on the carbon powder surface. We suspect that an electron donating >N: group near a Pt particle may help to keep H^+ ions closing to a Pt particle (Fig. 5b, 1st step of bottom interaction scheme). Increasing the pyridine function group of PyA monomer of PyPBI binder in the CL provides more electron donating >N: groups and helps attract the H^+ ions on the Pt active sites (Fig. 5b, 2nd and 3rd interaction scheme), thus improving the CV Pt-ECSA.

3.4. H_3PO_4 doping level of the GDEs

Before pressing with a PBI/epoxy cross-linked membrane for preparing MEAs, the anode and cathode GDEs (Pt loading was 0.5 mg cm^{-2}) were immersed in a 10 wt% H_3PO_4 aqueous solution

Table 3
Pt-ECSAs of GDEs (without doping H_3PO_4) consisting of PyPBI and PBI-11 catalyst binders. Pt loading 0.1 mg cm^{-2} . $[\text{PyPBI (or PBI)}]/[\text{PyPBI (or PBI)} + \text{Pt-C}] = 5\text{ wt.}\%$

Polyelectrolyte binder	Pt-ECSA/ $\text{m}^2\text{ g}^{-1}$
PyPBI-64	57 ± 2
PyPBI-55	54 ± 2
PyPBI-46	52 ± 1
PyPBI-37	50 ± 3
PBI-11	49 ± 2

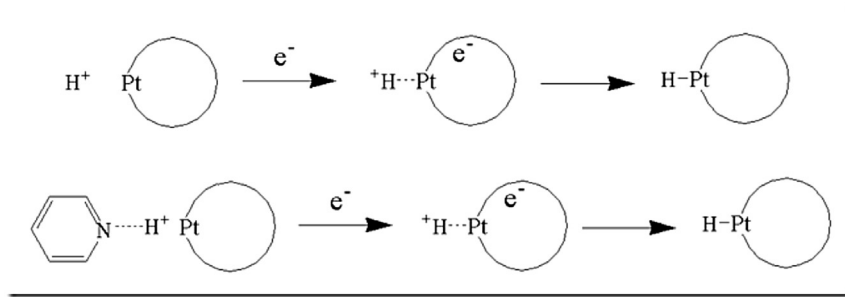


Fig. 5. The interaction of H^+ ion with the Pt particles on the surface of a carbon powder (the large sphere particle). (a. top scheme) A negatively charged electron on the carbon powder (2nd step) causes the attraction of an H^+ ion on to the surface of a Pt particle (3rd step). (b. bottom scheme) An electron donating $>\text{N}:$ group near a Pt particle helps to keep an H^+ ion closing to a Pt particle (1st step) and thus helps the attraction of the H^+ ions on the surfaces of a Pt particle.

at room temperature for 12 h. The H_3PO_4 loadings of the GDEs fabricated using catalyst ink solutions containing the four PyPBIs and the PBI-11 are summarized in **Table 4**. These data demonstrated that the H_3PO_4 loading of the GDE increased with increasing the PyA monomer content of PyPBI binder in the CL of a GDE. It is the lone pair electrons of the imidazole and pyridine $>\text{N}:$ groups providing the binding sites for the H_3PO_4 molecules. The increasing of the PyA monomer in the PyPBI binder led the PyPBI to have more $>\text{N}:$ groups for binding the H_3PO_4 molecules on the CL of the GDEs. Thus the H_3PO_4 loading of the GDE increased with the increase of the PyA monomer content of the PyPBI binder in CL.

3.5. PEMFC performance of MEAs

Unit cell PEMFC tests were performed at 160 °C with unhumidified H_2/O_2 and H_2/air gases under ambient pressure. **Figs. 6** and **7** illustrates the unit cell test *i*–*V* curves with unhumidified H_2/O_2 and H_2/air gases, respectively, of five MEAs prepared using Pt–C/DMAC catalyst ink solutions containing four PyPBIs and PBI-11 binders. The *i*–*V* curves of **Figs. 6** and **7** demonstrate that the fuel cell performance increased with the CL binder according to the sequence of PBI-11 < PyPBI-37 < PyPBI-46 < PyPBI-55 < PyPBI-64, that is, fuel cell performance increased with the increase of PyA monomer content of the PyPBI binder in CL.

To eliminate the change in cell performance due to the change in cell internal resistance, the *in situ* current interruption measurements were carried out to obtain the cell internal resistances, which comprise of the membrane ionic resistance and contact resistances. The cell internal resistances and the corresponding iR-free cell voltages vs. current density of **Fig. 6** (with H_2/O_2 fuel gases) after subtracting the performance loss from cell internal resistances are shown in **Fig. 8**. These results demonstrate that the cell internal resistance increased with the CL binder according to the sequence of PyPBI-64 < PyPBI-55 < PyPBI-46 < PyPBI-37 < PBI-11. Since all the MEAs were composed of a same PEM, the PEM ionic resistance should be same for all MEAs. As will be discussed in Section 3.6 (Impedances of MEAs), the difference in cell internal

resistance in these MEAs mainly came from the difference in the contact resistance between PEM and CL. **Fig. 8** also shows that the iR-free cell performance increased with the CL binder according to the sequence of PBI-11 ~ PyPBI-37 ~ PyPBI-46 < PyPBI-55 < PyPBI-64. However, compared to **Fig. 6**, the iR-free cell performances of these MEAs become much closer to each other once the difference in cell internal resistance is eliminated. The difference in performance left after the iR-free correction among these MEAs can be attributed to the difference in the PyA monomer content of the catalyst binder and the difference in H_3PO_4 doping level in CL (**Table 4**).

All these results were consistent with the GDE Pt-ECSA (**Fig. 4** and **Table 3**) and the CL H_3PO_4 loading data (**Table 4**). It is obvious that the increase of PyA monomer content of the PyPBI catalyst binder in CL increases the binding sites for H_3PO_4 and improves the fuel cell performance. The other possible reason for the better fuel cell performance of the MEAs consisting of higher PyA monomer content PyPBI catalyst binder can be attributed to the larger content of the electron donating $>\text{N}:$ group, which helps reduction of H^+ ions on the Pt active surface (**Fig. 5b**).

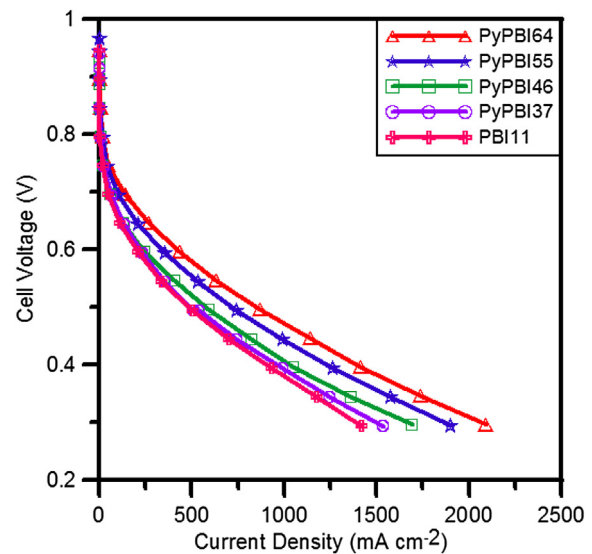


Fig. 6. Unit fuel cell test *i*–*V* curves of five MEAs fabricated using Pt–C catalyst ink solutions containing LiCl and four PyPBIs and PBI-11 (Pt–C/PyPBI (or PBI)/LiCl/DMAC = 9.5/0.5/0.5/190 by wt.). The Pt loadings were 0.5 mg cm^{-2} both at anode and cathode. The cell temperature was 160 °C with both the unhumidified H_2/O_2 flow rates of 200 mL min^{-1} and the active area of each MEA was $3.5 \times 3.5 \text{ cm}^2$. CL polyelectrolyte binders: (✚) PBI-11; (●) PyPBI-37; (■) PyPBI-46; (★) PyPBI-55; (▲) PyPBI-64.

Table 4

H_3PO_4 loadings of the anode and cathode GDEs (Pt loading 0.5 mg cm^{-2}) of MEAs consisting of PyPBI and PBI-11 catalyst binders.

GDE binder	H_3PO_4 loading in CL/ $\mu\text{mol cm}^{-2}$
PyPBI-64	11.3 ± 0.5
PyPBI-55	10.6 ± 0.4
PyPBI-46	9.4 ± 0.4
PyPBI-37	9.3 ± 0.3
PBI-11	6.0 ± 0.3

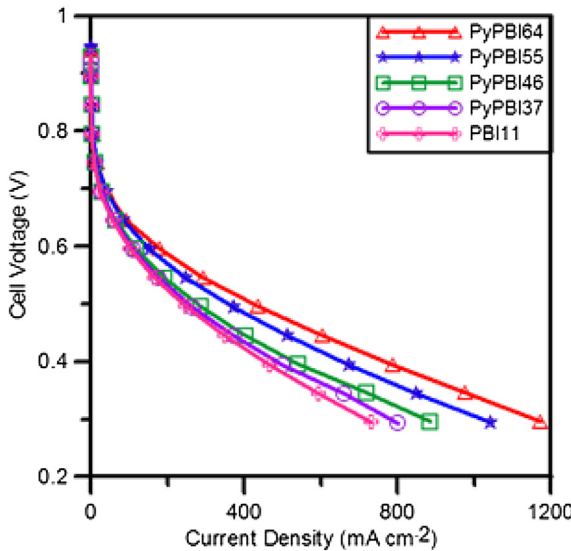


Fig. 7. Unit fuel cell test i – V curves of the same five MEAs as those shown in Fig. 6. The cell temperature was 160 °C with the unhumidified H₂ and air flow rates of 200 and 1000 mL min⁻¹, respectively. CL polyelectrolyte binders: (⊕) PBI-11; (○) PyPBI-37; (□) PyPBI-46; (★) PyPBI-55; (△) PyPBI-64.

3.6. Impedances of MEAs

AC impedance measurements were also conducted to investigate the resistance of the MEAs consisting of four PyPBIs and PBI-11 catalyst binders. The AC impedance diagrams were simulated using a Z-view program (Scribner Associates, Inc.) and fitted to an equivalent circuit (Fig. 9). The circuit consisted of a resistance R_s , which represents the total non-electrode cell ohmic resistance in series, a cathode charge transfer resistance R_{cC} , and an anode charge transfer resistance R_{cA} . R_{cC} and R_{cA} are parallel to the cathode constant phase element CPE_C and anode constant phase element CPE_A , respectively, which represent the cathode and anode porous electrode double layers, respectively [34–36].

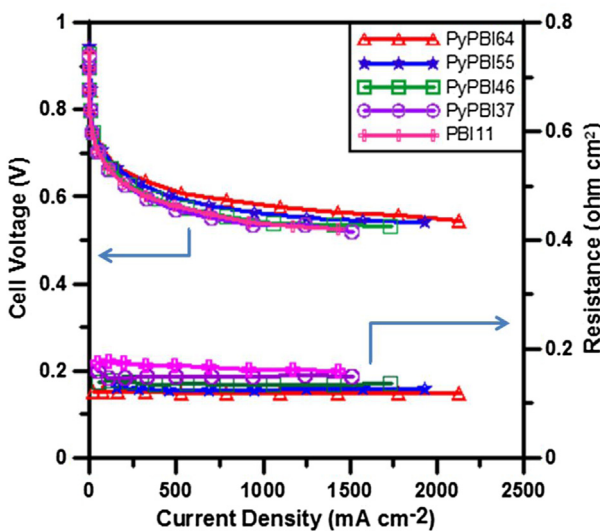


Fig. 8. Cell internal resistances and the corresponding plots of iR-free cell voltages vs. current density of Fig. 6 (with unhumidified H₂/O₂ fuel gases) after subtracting the performance loss from cell internal resistances. CL polyelectrolyte binders: (⊕) PBI-11; (○) PyPBI-37; (□) PyPBI-46; (★) PyPBI-55; (△) PyPBI-64.

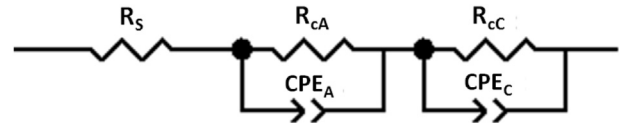


Fig. 9. An equivalent circuit model for a fuel cell impedance, where R_s represents total non-electrode cell ohmic resistance, R_{cA} and R_{cC} represent anode and cathode charge transfer resistances, respectively, and CPE_A and CPE_C represent anode and cathode porous double-layer capacitance, respectively.

In a fuel cell, the main contribution to R_s (the high frequency resistance) comes from the proton transport resistance of the membrane and the contact resistance between the PEM and the CL. Figs. 10 and 11 display the AC impedance diagrams obtained at a constant current $i = 200 \text{ mA cm}^{-2}$ and $i = 1000 \text{ mA cm}^{-2}$, respectively, with unhumidified H₂/O₂ fuel gases for MEAs consisting of PyPBIs and PBI-11 catalyst binders. Tables 5 and 6 summarize the R_s , R_{cA} , R_{cC} , and R_{CT} (where $R_{CT} = R_{cA} + R_{cC}$) values estimated from the impedance diagrams of Fig. 10 (i.e., at $i = 200 \text{ mA cm}^{-2}$) and Fig. 11 (i.e., at $i = 1000 \text{ mA cm}^{-2}$), respectively, simulated using the equivalent circuit shown in Fig. 9. Figs. 10 and 11, Table 5, and Table 6 revealed that both the R_s values at $i = 200 \text{ mA cm}^{-2}$ and 1000 mA cm^{-2} varied with the variation of the catalyst binder in the CLs according to the sequence of PBI-11 > PyPBI-37 > PyPBI-46 > PyPBI-55 > PyPBI-64. These results were quite consistent with the unit cell i – V data and cell internal resistance data presented in Fig. 6. These results were also consistent with the GDE H₃PO₄ loading results shown in Table 4, that is, the MEA with a higher GDE H₃PO₄ loading had a lower R_s value. As all the MEAs were composed of a same PEM, the proton transfer resistance from PEM should be same for all the MEAs. The differences in R_s (Tables 5 and 6) and in cell internal resistance (Fig. 6) in these MEAs might come from the difference in the contact resistance between the PEM and CL. The increase of the PyA monomer content in the PyPBI catalyst binder caused an increase in the CL H₃PO₄ loading (Table 4), which led to a better contact between PEM and CL and a lower R_s (Tables 5 and 6). These data also show that the R_{CT} of the MEAs decreased according to the sequence of PBI-11 > PyPBI-37 > PyPBI-46 > PyPBI-55 ~ PyPBI-64 at a low current (i.e., $i = 200 \text{ mA cm}^{-2}$, Table 5) and PBI-11 > PyPBI-

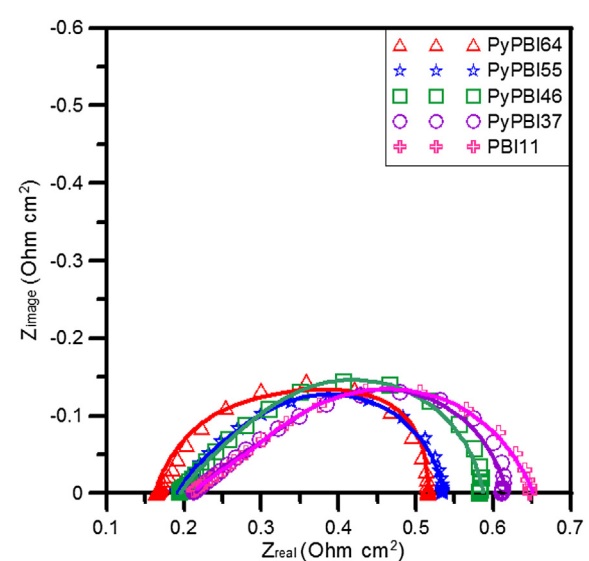


Fig. 10. Impedances of MEAs at $i = 200 \text{ mA cm}^{-2}$ after activating for 8 h. CL polyelectrolyte binders: (⊕) PBI-11; (○) PyPBI-37; (□) PyPBI-46; (★) PyPBI-55; (△) PyPBI-64.

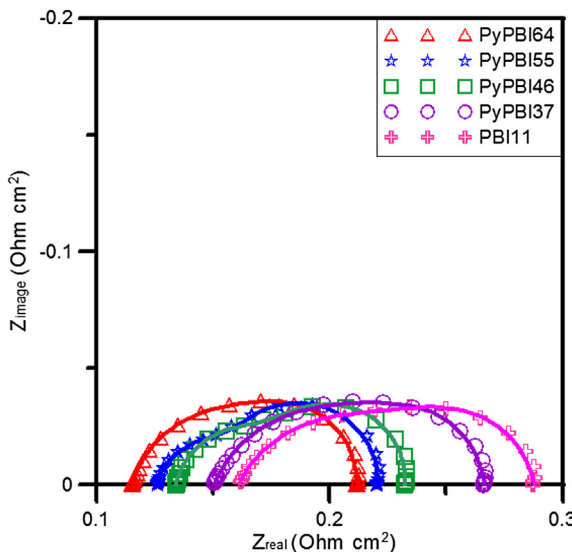


Fig. 11. Impedances of MEAs at $i = 1000 \text{ mA cm}^{-2}$ after activating for 8 h. CL poly-electrolyte binders: (✚) PBI-11; (○) PyPBI-37; (□) PyPBI-46; (★) PyPBI-55; (△) PyPBI-64.

$37 > \text{PyPBI-46} \sim \text{PyPBI-55} \sim \text{PyPBI-64}$ at a high current (i.e., $i = 1000 \text{ mA cm}^{-2}$, Table 6).

Table 4 shows that the GDE H_3PO_4 loading of the MEA consisting of PBI-11 catalyst binder was much smaller than those of the MEAs consisting of PyPBI catalyst binders, which might cause a much larger R_{CT} of the MEA consisting of PBI-11 catalyst binder than those consisting of PyPBI catalyst binders. The small difference in the GDE H_3PO_4 loadings of the MEAs consisting of PyPBI-46, PyPBI-55, and PyPBI-64 might be the reason for the small difference in the R_{CT} s of the MEAs consisting of PyPBI-46, PyPBI-55, and PyPBI-64 catalyst binders. The larger H_3PO_4 loading may reduce the proton transfer resistance in CL; however, the larger H_3PO_4 loading may also lead to a larger amount of H_3PO_4 covering on the Pt particle surfaces, resulting in a lower Pt catalysis activity. This may be the another reason for the similar R_{CT} s of the MEAs consisting of PyPBI-46, PyPBI-55, and PyPBI-64 catalyst binders. From Tables 4 and 5, we also found that there was no much difference between the R_{CA} value at $i = 200 \text{ mA cm}^{-2}$ and at $i = 1000 \text{ mA cm}^{-2}$ for a same MEA. For a same MEA at a low current $i = 200 \text{ mA cm}^{-2}$, the R_{CA} value was much smaller than the R_{CC} value and the main contribution to the R_{CT} mainly came from R_{CC} . However, for an MEA at a high current $i = 1000 \text{ mA cm}^{-2}$, the R_{CA} value may play an important role in the R_{CT} because of the lower R_{CC} value at a higher current.

4. Conclusions

The CL of PBI/ H_3PO_4 -based HT-PEMFC MEAs consists of a Pt–C catalyst, H_3PO_4 electrolyte, and PBI (or PyPBI) binder, wherein the Pt particles act as active sites for electrochemical reactions, the H_3PO_4 molecules serve as proton conductors, and PBI (or PyPBI)

Table 5

R_s , R_{CA} , R_{CC} , and R_{CT} ($R_{CT} = R_{CA} + R_{CC}$) at $i = 200 \text{ mA cm}^{-2}$ of MEAs consisting of PyPBI and PBI-11 catalyst binders.

Binder	R_s ($10^{-2} \Omega \cdot \text{cm}^2$)	R_{CA} ($10^{-2} \Omega \cdot \text{cm}^2$)	R_{CC} ($10^{-2} \Omega \cdot \text{cm}^2$)	R_{CT} ($10^{-2} \Omega \cdot \text{cm}^2$)
PyPBI-64	16.3 ± 0.4	3.1 ± 0.3	32.1 ± 0.5	35.2 ± 0.8
PyPBI-55	18.9 ± 0.5	2.7 ± 0.3	31.8 ± 0.5	34.5 ± 0.8
PyPBI-46	19.2 ± 0.6	3.9 ± 0.4	35.1 ± 0.5	39.0 ± 0.9
PyPBI-37	20.9 ± 0.6	2.9 ± 0.3	37.3 ± 0.7	40 ± 1
PBI-11	20.9 ± 0.6	4.1 ± 0.4	40.1 ± 0.8	44 ± 1

Table 6

R_s , R_{CA} , R_{CC} , and R_{CT} ($R_{CT} = R_{CA} + R_{CC}$) at $i = 1000 \text{ mA cm}^{-2}$ of MEAs consisting of PyPBI and PBI-11 catalyst binders.

Binder	R_s ($10^{-2} \Omega \cdot \text{cm}^2$)	R_{CA} ($10^{-2} \Omega \cdot \text{cm}^2$)	R_{CC} ($10^{-2} \Omega \cdot \text{cm}^2$)	R_{CT} ($10^{-2} \Omega \cdot \text{cm}^2$)
PyPBI-64	11.6 ± 0.2	2.2 ± 0.2	7.6 ± 0.2	9.8 ± 0.4
PyPBI-55	12.6 ± 0.3	1.8 ± 0.2	7.6 ± 0.3	9.4 ± 0.5
PyPBI-46	13.4 ± 0.3	2.5 ± 0.2	7.3 ± 0.3	9.8 ± 0.5
PyPBI-37	15.0 ± 0.4	3.8 ± 0.3	7.8 ± 0.4	11.6 ± 0.7
PBI-11	16.1 ± 0.4	3.8 ± 0.3	8.8 ± 0.4	12.6 ± 0.7

binds together the Pt–C particles, the PEM, and the GDLs. The PBI (or PyPBI) binder also helps fixing H_3PO_4 molecules to avoid H_3PO_4 molecules leakage from CL to GDL. In present study, we prepared HT-PEMFC MEAs using low MW ($M_w = 1.0\text{--}1.3 \times 10^{-4} \text{ g mol}^{-1}$) PBI-11 and PyPBIs as catalyst binders. We demonstrated that increasing the PyA/IPA monomer mole ratio of the PyPBI catalyst binder from 0/1 to 6/4 resulted in an increase in the CL H_3PO_4 loading; this reduced the contact resistance between the PEM and the CL and thus reduced the R_s of the MEAs. The increase of CL H_3PO_4 loading also caused a reduction of R_{CT} according to the sequence of the catalyst binder PBI-11 > PyPBI-37 > PyPBI-46 ~ PyPBI-55 ~ PyPBI-64. The high H_3PO_4 loading in CL might reduce the resistance of proton transfer in CL. However the high H_3PO_4 loading might also lead to excess H_3PO_4 covering on the surfaces of the Pt particles and reduced Pt-active surface area. The single cell test results demonstrated that the fuel cell performance decreased according to the sequence of the catalyst binder of PBI-11 > PyPBI-37 > PyPBI-46 > PyPBI-55 > PyPBI-64, which was consistent with the combination of the R_s and R_{CT} .

Acknowledgment

The authors would like to thank the National Science Council (NSC), Taiwan for financial support through grant NSC-100-2221-E-155-009-MY3.

References

- [1] J.S. Wainright, J.T. Wang, D. Weng, R.F. Savinell, M.H. Litt, *J. Electrochem. Soc.* 142 (1995) L121–L123.
- [2] J.T. Wang, R.F. Savinell, M.H. Litt, H. Yu, *Electrochim. Acta* 41 (1996) 193–197.
- [3] M. Rikukawa, K. Sanui, *Prog. Polym. Sci.* 25 (2000) 1463–1502.
- [4] K.D. Kreuer, *J. Membr. Sci.* 185 (2001) 29–39.
- [5] P.D. Genova, *J. Membr. Sci.* 185 (2001) 59–71.
- [6] Q.F. Li, R.H. He, J.O. Jensen, N.J. Bjerrum, *Chem. Mater.* 15 (2003) 4896–4915.
- [7] M.A. Hickner, H. Ghassemi, Y.S. Kim, B.R. Einstla, J.E. McGrath, *Chem. Rev.* 104 (2004) 4587–4611.
- [8] Q.F. Li, J.O. Jensen, R.F. Savinell, N.J. Bjerrum, *Prog. Polym. Sci.* 34 (2009) 449–477.
- [9] H. Vogel, C.S. Marvel, *J. Polym. Sci. Part A Polym. Chem.* 34 (1996) 1125–1153.
- [10] J. Larminie, A. Dicks, *Fuel Cell Systems Explained*, John Wiley & Sons, Ltd., Chichester, England, 2000 (Chapter 4).
- [11] F. Barbir, *PEM Fuel cells – Theory and practice*, Elsevier, Burlington, MA, 2005 (Chapter 3).
- [12] C. Wannek, I. Konradi, J. Mergel, W. Lehnert, *Int. J. Hydrogen Energy* 34 (2009) 9479–9485.
- [13] C. Wannek, W. Lehnert, J. Mergel, *J. Power Sources* 192 (2009) 258–266.
- [14] J. Lobato, P. Canizares, M.A. Rodrigo, J.J. Linares, F.J. Pinar, *Int. J. Hydrogen Energy* 35 (2010) 1347–1355.
- [15] Y. Kwon, T.Y. Kim, D.Y. Yoo, S.G. Hong, J.O. Park, *J. Power Sources* 188 (2009) 463–467.
- [16] Q.F. Li, R.H. He, J.A. Gao, J.O. Jensen, N.J. Bjerrum, *J. Electrochem. Soc.* 150 (2003) A1599–A1605.
- [17] J.A. Asensio, S. Borro, P. Gomez-Romero, *J. Electrochem. Soc.* 151 (2004) A304–A310.
- [18] A. Su, Y.M. Ferng, X.Y. Tsai, *Int. J. Energy Res.* 37 (2013) 1213–1222.
- [19] S. Kaserer, K.M. Caldwell, D.E. Ramaker, C. Roth, *J. Phys. Chem.* 117 (2013) 6210–6217.
- [20] M. Mamlouk, K. Scott, *Int. J. Hydrogen Energy* 35 (2010) 784–793.
- [21] S. Matar, A. Higier, H. Liu, *J. Power Sources* 195 (2010) 181–184.
- [22] P. Zelenay, B.R. Scharifker, J.O.M. Bockris, D. Gervasio, *J. Electrochem. Soc.* 133 (1986) 2262–2267.

- [23] Q.F. Li, H.A. Hjuler, N.J. Bjerrum, *J. Appl. Electrochem.* 31 (2001) 773–779.
- [24] H.L. Lin, Y.C. Chen, C.C. Li, C.P. Cheng, T.L. Yu, *J. Power Sources* 181 (2008) 228–236.
- [25] P.H. Su, H.L. Lin, Y.P. Lin, T.L. Yu, *Int. J. Hydrogen Energy* 38 (2013) 13742–13753.
- [26] Q. Li, J.O. Jensen, C. Pan, V. Bandur, M.S. Nilsson, F. Schönberger, *Fuel Cells* 8 (2008) 188–199.
- [27] H.L. Lin, Y.C. Chou, T.L. Yu, S.W. Lai, *Int. J. Hydrogen Energy* 37 (2012) 383–392.
- [28] Y. Iwakura, K. Uno, Y. Imai, *J. Polym. Sci. A* 2 (1964) 2605–2615.
- [29] T.J. Schmidt, H.A. Gasteiger, G.D. Ståb, P.M. Urban, D.M. Kolb, R.J. Behm, *J. Electrochem. Soc.* 145 (1998) 2354–2358.
- [30] L. Colombi Ciacchi, W. Pompe, A. De Vita, *J. Phys. Chem. B* 107 (2003) 1755–1764.
- [31] F. Barbir, *PEM Fuel Cells: Theory and Practice*, Elsevier Academic Press, Burlington, MA, 2005 (Chapter 8).
- [32] D.L. Pavia, G.M. Lampman, G.S. Kriz, *Introduction to Spectroscopy: A guide for Students of Organic Chemistry*, Saunders College Publishing, Philadelphia, PA, 1979 (Chapter 2).
- [33] R.M. Silverstein, G.C. Bassler, T.C. Morrill, *Spectrometric Identification of Organic compounds*, fourth ed, John Wiley & Sons, New York, 1981 (Chapter 3).
- [34] K.R. Cooper, V. Ramani, J.M. Fenton, H.R. Kunz, *Experimental Methods and Data Analyses for Polymer Electrolyte Fuel Cells*, Scribner Associates, Inc., North Carolina, 2006. Laboratory #5 – Impedance spectroscopy of PEM fuel cells.
- [35] S.J. Andresaen, J.L. Jespersen, E. Schaltz, S.K. Kaer, *Fuel Cells* 4 (2009) 463–473.
- [36] M. Ciureanu, R. Roberge, *J. Phys. Chem. B* 105 (2001) 3531–3539.